

# $^{88}\text{Sr}^+$ Ion Trap Apparatus for Generating 408 nm Photons

Jianlong Lin,<sup>1</sup> Mari Cieszyński,<sup>2</sup> William Christopherson,<sup>2</sup> Darman Khan,<sup>2</sup> Lintao Li,<sup>2</sup> Elizabeth Goldschmidt,<sup>2</sup> and Brian DeMarco<sup>2</sup>

<sup>1</sup>*Department of Electrical and Computer Engineering, University of Illinois Urbana-Champaign, Urbana, IL, USA*

<sup>2</sup>*Department of Physics, University of Illinois Urbana-Champaign, Urbana, IL, USA*

(\*Electronic mail: [bdemarco@illinois.edu](mailto:bdemarco@illinois.edu))

(Dated: 30 June 2025)

We describe a  $^{88}\text{Sr}^+$  ion trap apparatus with the capability to produce high-quality 408 nm photons aimed at distributed quantum computing and networking applications. This instrument confines ion chains using a surface electrode trap with a two-dimensional magneto-optical trap as an atomic source. Several laser systems spanning 400–1100 nm are used to achieve high fidelity state preparation and readout. Photons are produced via the decay of an excited state, which is accessed using a custom 408 nm laser system that produces 150 ps optical pulses using non-linear photonics. We demonstrate single photon production through a Hanbury Brown-Twiss measurement for one to six ions.

## I. INTRODUCTION

Establishing high-fidelity entanglement between separated quantum bits (qubits) in a quantum network generally requires reliable, coherent control of quantum light–matter interfaces. Quantum information must be converted from a “stationary” qubit, held in one or more matter-based qubits, into a “flying” qubit encoded in a single photon or other quantum state of light<sup>1,2</sup>. One promising paradigm for such an interface is a single emitter with internal spin structure that can be induced to emit a single photon whose state is entangled with its spin state. The potential functionality of such a system expands greatly when the emitter can be part of a larger quantum register comprised of multiple qubits, such as neutral atoms or trapped atomic ions<sup>3,4</sup>.

Another important feature required for high-fidelity entanglement distribution is that the emitter produces photons in a well-defined quantum state, which can be difficult to achieve in practice. Many solid-state emitters, for example, produce light with a multiphoton background<sup>5</sup>, with excess spectral broadening due to dephasing during the emission time<sup>6,7</sup>, or such that subsequent photons are not spectrally identical<sup>8,9</sup>.

Here, we demonstrate the development of an instrument to trap  $^{88}\text{Sr}^+$  ions as a high quality light–matter interface to 408 nm photons. We show suppression of multiphoton emission to the level of  $10^{-3}$ . While we do not directly measure the spectral purity in this work, we expect to be able to achieve high indistinguishability due to the nature of trapped ions being identical in vacuum<sup>10</sup>. The architecture is compatible with implementing quantum circuits for quantum information processing after entanglement distribution via single and two-qubit gates within a register<sup>4</sup>.

## II. ION TRAPPING APPARATUS

In this section, we describe the design and implementation of the instrument that is used to trap  $^{88}\text{Sr}^+$  atomic ions, prepare their quantum state, and produce fast 408 nm excitation pulses to generate photons that are collected via an imaging system. The equipment includes an ultra-high vacuum sys-

tem, continuous-wave lasers and associated optical systems, imaging optics and detectors, and a custom 150 ps pulsed laser system.

### A. Vacuum system

The ultra-high vacuum (UHV) system we have built is designed to provide an environment for chip-based ion trap experiments. We use a surface electrode trap designed and fabricated by the Massachusetts Institute of Technology Lincoln Laboratory (MIT LL) Quantum Computing Laboratory team. This trap can confine ions in three separate regions situated along the axial direction and is similar to the device described in Ref. 11. Our variation is composed of niobium conducting electrodes deposited on a sapphire substrate, with 11-electrode pairs along the axial direction of the trap. We trap ions in just one zone for the experiments described in this manuscript. Using a simulation of the trap potential, we selected a set of RF and DC voltages to produce approximately 1.3 MHz axial and 4 MHz radial trap frequencies, with the radial principal axes tilted by approximately 30 degrees relative to the plane of the trap.

The UHV system, shown in Fig. 1, is composed of two chambers separated by a gate valve. In one chamber we generate an isotope-selective, two-dimensional magneto-optical trap (2D MOT) of  $^{88}\text{Sr}$  atoms, and in the other we trap and manipulate  $^{88}\text{Sr}^+$  atomic ions. The 2D MOT is used to enable fast loading from a pre-cooled source of atoms<sup>11,12</sup>. This approach avoids depositing unwanted material onto the trap surface. The 2D MOT uses a heated metal source to create a vapor of Sr atoms and is a  $^{88}\text{Sr}$  variation of the design described in Ref. 13. After generating the 2D MOT, a laser beam pushes the atoms to the second chamber, where they are ionized and trapped.

The UHV environment is maintained using a Gifford-McMahon cryocooler (Lakeshore Cryotronics low-vibration SHI-4XG-UHV-15). The cryocooler enables a wide range of materials to be used in the vacuum system and rapid swapping of components without the need to bake at high temperature to achieve UHV. Also, the ion trap chip is connected to the

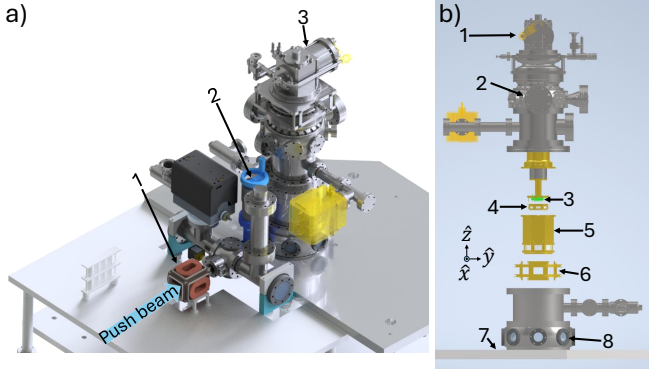


FIG. 1. Vacuum system design. (a) A rendered model showing the full assembly: (1) 2D MOT glass cell and coils, (2) gate valve, and (3) cold head. (b) An exploded view showing the inside of the vacuum system surrounding the cryostat: (1) cold head, (2) feed-throughs for wiring, (3) trap assembly, (4) 4 K radiation shield, (5) 50 K radiation shield, (6) magnetic field coils, (7) breadboard with 6.2 inch bore for imaging, and (8) viewports for beam delivery. The wiring has been excluded for simplicity.

cryocooler cold finger, which reduces the anomalous ion motion heating rate<sup>14</sup>. A temperature of approximately 4 K is achieved at our trap at the cryocooler base temperature. The design of this system is a variation of that described in Ref. 11. Our system, as shown in Fig. 1, includes two changes compared with previous designs: an optical breadboard that supports the vacuum system, and vector magnetic field coils that are located inside the vacuum system.

By mounting the vacuum system to a custom breadboard, the ion addressing optics are mechanically coupled to the vacuum system, and thereby to the trap. This design minimizes the intensity and phase fluctuations that individual ions experience from the addressing beams due to mechanical vibrations. The optics for laser beam delivery are mounted to this breadboard and direct each beam through a viewport (Kurt J. Lesker VPZL-275) to manipulate ions located beneath the trap. This custom 1.5 inch thick aluminum optical breadboard also has a 6.2 inch bore cut out to provide optical access for the imaging system.

Three-dimensional (3D) in-vacuo magnetic field coils provide a static field of approximately 0.5 mT; similar designs have previously been used to provide a magnetic field along just one direction<sup>11,15</sup>. A 3D model of the coils, along with the principal directions of the magnetic field, are shown in Fig. 1. These coils provide 3D control over the magnetic field at the ions in a compact package. The magnetic field coils are composed of custom electro-polished, gold-plated, oxygen-free high thermal conductivity (OFHC) copper coil holders wound with polyimide-coated copper magnet wire. The coils are encapsulated in Stycast 2850FT with Catalyst 9. The coils that generate magnetic fields in the  $\hat{x}$  and  $\hat{y}$  directions (i.e., in the plane of the ion-trap chip) are wound with 108 turns of 22 AWG wire, and the pair that generates a magnetic field in  $\hat{z}$  (i.e., orthogonal to the plane of the surface trap) is wound with 56 turns of 20 AWG wire. Producing a 0.5 mT field requires 0.8 A ( $\hat{z}$  pair) and 1.7 A ( $\hat{x}$  and  $\hat{y}$  pairs) currents. The

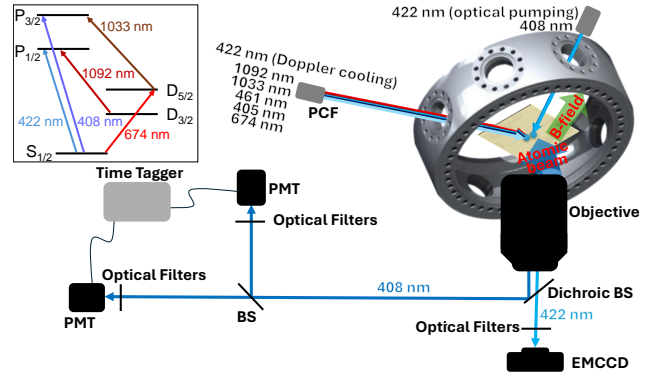


FIG. 2. Diagram showing laser-beam geometry used to manipulate trapped ions and the imaging system that collects fluorescence. Two optical systems deliver focused laser light to the trapping zone. An NA  $\approx$  0.48 objective collects ion fluorescence and directs it to a Hanbury-Brown and Twiss (HBT) measurement setup. Inset: energy level diagram of  $^{88}\text{Sr}^+$  showing the laser wavelengths used to address transitions between quantum states.

coil holders connect directly to the 50 K radiation shield, with enough surface area to ensure sufficient thermal contact. For our setup, the magnetic field is configured to be pointing in the  $-\hat{y}$  direction indicated in Fig. 1(b) at the trapping location.

## B. Laser systems for trapping, state preparation, and measurement

Several laser beams at different wavelengths are needed to trap ions and for state preparation and measurement. A diagram of the laser beam geometry and energy levels of  $^{88}\text{Sr}^+$  is shown in Fig. 2. The acousto-optic modulators (AOMs) used to turn these laser beams on and off during data collection are not shown.

To trap ions, we follow the method described in Ref. 11. A 461 nm beam resonant with the  $^1S_0 \leftrightarrow ^1P_1$  transition in neutral  $^{88}\text{Sr}$  pushes atoms from the 2D MOT to the ion trap chip. An additional 461 nm beam (20  $\mu\text{W}$ , linearly polarized relative to the magnetic field) combines with a 405 nm beam (800  $\mu\text{W}$ ,  $\sigma^{+/-}$ -polarized) at the trapping region to photoionize  $^{88}\text{Sr}$ . The push beam has a waist (i.e.,  $1/e^2$  radius) of 1 mm, which is large enough to supply ions to any trapping region. To selectively load to the desired zone, the photoionization beam, which propagates at a 90/45 degree angle to the neutral atom beam/axial direction, is focused to a waist of approximately 30  $\mu\text{m}$ . The 461 nm beams used for the 2D-MOT, push beam, and photoionization are produced by an external cavity diode laser (ECDL, Toptica DL pro HP 461). The 405 nm second-stage photoionization beam is produced by a Toptica iBEAM-SMART-405-S-HP.

The 0.5 mT magnetic field lifts the degeneracy of the  $S_{1/2}$  manifold to the  $|\downarrow\rangle \equiv |S_{1/2}, m_j = -1/2\rangle$  and  $|\uparrow\rangle \equiv |S_{1/2}, m_j = +1/2\rangle$  sublevels, which is referred to as the Zeeman qubit. The ions are prepared for single photon emission at 408 nm on the closed  $|\downarrow\rangle \leftrightarrow |P_{3/2}, m_j = -3/2\rangle$  transition, first by Doppler cooling and optical pumping. Doppler cool-

ing is implemented using a few  $\mu\text{W}$  of  $\pi$ -polarized 422 nm light to drive the  $S_{1/2} \leftrightarrow P_{1/2}$  transition. The ions are then optically pumped to the  $|\downarrow\rangle$  state using a few  $\mu\text{W}$  of  $\sigma^-$ -polarized 422 nm light. The 422 nm light is derived from an external cavity diode laser (ECDL, Toptica DL pro HP 420). Light to quench atoms from the metastable  $D_{3/2}$  and  $D_{5/2}$  states, which have a small branching ratio for decay from the  $P_{1/2}$  and  $P_{3/2}$  states, is produced by a 1092 nm laser (Toptica DL pro using diode LD-1120-0100-AR-2) and a 1033 nm laser (Toptica DL pro using diode LD-1060-0200-AR-2). Approximately 20  $\mu\text{W}$  of 1092 nm  $\sigma^{+/-}$ -polarized light and 3  $\mu\text{W}$  of 1033 nm  $\sigma^{+/-}$ -polarized light is used for quenching.

To optimize and characterize the state preparation and measurement (SPAM) fidelity, we use spin-state selective readout to distinguish between  $|\downarrow\rangle$  and  $|\uparrow\rangle$  via fluorescence on the  $S_{1/2} \leftrightarrow P_{1/2}$  transition<sup>16</sup>. The population in  $|\downarrow\rangle$  is first shelved to the metastable  $D_{5/2}$  manifold using a narrow-linewidth ( $<10$  Hz) laser at 674 nm so that the  $|\downarrow\rangle$  state does not fluoresce under exposure to 422 nm light. We use approximately 1 mW of 674 nm light polarized orthogonally to the magnetic field to drive  $\Delta m_j = \pm 2$  transitions. To estimate the fidelity of optical pumping and shelving separately, we apply a double-shelving technique. We first measure the combined optical pumping, shelving, and readout fidelities after applying separate experimental sequences to only shelve to  $|D_{5/2}, m_j = -5/2\rangle$  or  $|D_{5/2}, m_j = +3/2\rangle$  using  $\pi$  pulses. We then employ a sequence that applies two  $\pi$  pulses, consecutively resonant with the  $|\downarrow\rangle \rightarrow |D_{5/2}, m_j = -5/2\rangle$  and  $|\downarrow\rangle \rightarrow |D_{5/2}, m_j = +3/2\rangle$  transitions, and measure the combined fidelity of this double-shelving sequence. By factorizing the optical pumping and individual shelving probabilities, and estimating the overall fidelity for each sequence, we isolate our fidelities for optical pumping and for the  $|\downarrow\rangle \rightarrow |D_{5/2}, m_j = -5/2\rangle$  and  $|\downarrow\rangle \rightarrow |D_{5/2}, m_j = +3/2\rangle$  shelving transitions. Here, we neglect the small decay probability from  $D_{5/2}$  to  $S_{1/2}$ . We estimate a combined optical pumping and readout fidelity of  $> 99\%$ , optimized by adjusting the magnetic field coil currents to align the static magnetic field to be parallel with the optical pumping beam and by optimizing the circular polarization purity. Because the 422 nm optical pumping beam and 408 nm beam used for single-photon schemes co-propagate, the magnetic field alignment optimizes the  $\sigma^-$  polarization of both beams.

The laser wavelengths are stabilized in several ways. The 422 nm laser is locked to the  $5P_{1/2} \leftrightarrow 6P_{1/2}$  transition in  $^{85}\text{Rb}$  via saturated absorption spectroscopy<sup>17</sup> in a heated rubidium vapor cell (Thorlabs GC25075-RB with GCH25R). An AOM (Isomet M1250-T250L-0.45) in a double-passed configuration is used to shift the 422 nm beam to near resonance. The 461 nm, 1033 nm, 1092 nm, and 816 nm ECDLs are frequency-stabilized using measurement by a wavelength meter (HighFinesse WS8-10) and feedback to the ECDL gratings. The 674 nm light is produced by a custom narrow-linewidth laser system from Stable Laser Systems (SLS-674-300-1) composed of an ECDL (Toptica DL pro 670) stabilized to a high-finesse optical cavity via the Pound-Drever-Hall technique. The light from a laser diode (Toptica Eagleyard EYP-RWE-0670-00703-1000-SOT02-0000) injection

locked to the 300  $\mu\text{W}$  transmitted output of the cavity is amplified using a tapered amplifier (TA) (BoostTA Pro-3V0). Two AOMs (Gooch & Housego 3200-1214) are used to shift this beam to resonance.

The photoionization, Doppler cooling, shelving, and metastable state repumping beams are joined together using dichroic beamsplitters into a constant mode-field diameter fiber photonic-crystal fiber (PCF) (NKT Photonics aeroGUIDE-5-PM). The output of this fiber is focused on the ions using silver-coated parabolic mirrors. This is an adaptation of a design used by MIT LL<sup>18</sup> and is constructed to focus the laser beams with different wavelengths to the same location. The waists of these beams at the focus ranges from 31  $\mu\text{m}$  to 43  $\mu\text{m}$ . To characterize the performance, we measure the location of the foci at 405 nm and 1092 nm ex-situ. Along the optical axis, the foci are shifted by 1.4 mm, and perpendicular to the axis they are shifted by less than 9  $\mu\text{m}$ . These distances are small compared with the shortest Rayleigh length and the beam waists, respectively. The  $\sigma^-$ -polarized 422 nm optical pumping and 408 nm excitation pulse beams (see Section II D) are delivered through a single-mode, polarization-maintaining fiber and similar focusing optics, with a polarizing beam splitter and a half- and a quarter-waveplate placed before the focusing mirror.

### C. Imaging system for photon collection and ion readout

The setup for ion imaging and photon collection and state readout is shown in Fig. 2. To collect fluorescence at 422 nm for readout and single photons at 408 nm from the ions, we use a 0.48 numerical aperture (NA) objective (Sill SS6ASS2258)<sup>11</sup>, which was custom-designed for these wavelengths. After the objective, a dichroic beamsplitter (Semrock FF414-Di01) directs the 422 nm and 408 nm light along separate imaging paths. The 422 nm light is steered to an Electron-Multiplying Charge-Coupled Device (EMCCD) camera (Andor iXon Ultra 888) for state readout between ground states of the  $S_{1/2}$  manifold and to check if ions are trapped. The 408 nm light emitted from the ion is sent through a Hanbury Brown and Twiss (HBT) setup to measure single-photon purity. The HBT setup employs photomultiplier tube (PMT) detectors (Hamamatsu H10682-210) along with a time-correlated single-photon counting module (Swabian Time Tagger Ultra) for coincidence measurements. Spectral filters ensure that unwanted light does not reach the EMCCD (one Semrock FF01-420/5-25 and one Semrock BSP01-633R-25) or PMTs (two Semrock ET402/15x and one Semrock FF01-492/SP-25).

### D. 408 nm pulsed laser system

To generate single photons for use as a spin-photon interface and for future entanglement schemes, we excite the ion from  $|\downarrow\rangle$  to the  $|e\rangle \equiv |P_{3/2}, m_j = -3/2\rangle$  state using a custom 408 nm pulsed-laser system. To ensure a high probability of producing only a single photon, the excitation pulse must be shorter than the  $\tau = 6.99$  ns excited state lifetime<sup>19,20</sup>. We



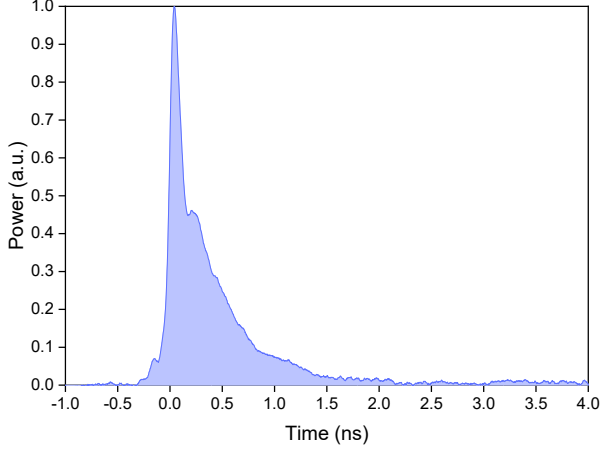


FIG. 3. Normalized output of the 408 nm pulsed system, measured using an oscilloscope and photodiode with 12.5 GHz bandwidths. The pulse has a FWHM of  $148 \pm 3$  ps, set by the electronic pulse generation circuit. The RF amplifier (Analog Devices EVAL-HMC998APM5E) used to drive the EOM broadens the tail at the end of the pulse.

have constructed a laser system capable of producing 150 ps 408 nm pulses to satisfy this criterion.

To generate 408 nm laser pulses, we use a CW 816 nm custom ECDL built using a laser diode (Thorlabs L820P200), which is chopped by a fast electro-optic modulator (EOM) and then frequency doubled (Fig. 4). The EOM (AdvR WPR-K0816) is a KTP-based waveguide device with an 18 pF input capacitance. It is used as an amplitude modulator, with a polarizer (Corning Polarcor) before the input fiber and a polarizing beamsplitter (Thorlabs PBS122) after the output fiber. The EOM is driven using a custom electrical pulse generation circuit based on a bias-switching step-recovery diode<sup>21</sup>. Further details and a circuit diagram can be found in Appendix A. The output of the EOM is amplified by a TA (Coherent I14N-TA-0820-2000-DHP) and then frequency doubled using a fiber-coupled lithium niobate waveguide device (AdvR RSH-M0408). The doubled pulse is focused onto the ions via the optics used for optical pumping, with  $\sigma^-$  polarization and a beam waist of approximately 20  $\mu\text{m}$ . We have implemented multiple stages of active stabilization to minimize optical power leakage through the EOM. These feedback systems are shown in the blue, green, and magenta blocks of Fig. 4 and are described in further detail in Appendix B.

We measure the ratio between the peak optical pulse power and background light leakage when no electrical pulse is applied to the EOM. We record the average 408 nm power at the doubler output with a power meter probe (Thorlabs S121C, specified with  $\pm 3\%$  measurement uncertainty at 408 nm) and vary the pulse repetition rate. Linear fitting produces a slope and intercept that correspond to a pulse energy of  $19.1 \pm 0.2 \mu\text{W}/\text{MHz} = 19.1 \pm 0.2 \text{ pJ}$  and a CW background power of  $1.92 \pm 0.04 \mu\text{W}$ , respectively. We then measure the pulse power versus time using a GaAs photodiode (EOT ET-

4000) and an oscilloscope (Tektronix MSO 71254C) with 12.5 GHz bandwidths (Fig. 3). We collect a small fraction of the optical power onto the photodiode, and to find the peak power we vertically scale this trace such that the integral of the pulse trace equals the pulse energy found from the average power measurements. For a sample of seven 128-average traces, the standard deviation of the integrated pulse energy is 7%. This gives a peak power of  $52 \pm 4 \text{ mW}$  and extinction ratio  $> 43 \text{ dB}$ .

The extinction ratio at the frequency doubler output is limited because the amplified spontaneous emission (ASE) from the TA is doubled. Due to the narrow phase-matching condition of the doubler, the spectrally broad ASE has low conversion efficiency. Despite this high attenuation, unwanted excitation of the ion would occur because of the low duty cycle. To mitigate this effect, we apply an 80 ns gate using an acousto-optic modulator (Isomet M1250-T250L-0.45), increasing the final extinction ratio to 55 dB.

### III. SINGLE PHOTON PURITY MEASUREMENT

To characterize the single-photon purity, we measured the normalized second-order auto-correlation function  $g^{(2)}(\tau)$  following the 408 nm excitation pulse. A perfect single photon source exhibits  $g^{(2)}(0) = 0$ , and any value of  $g^{(2)}(0) < 1$  implies suppression of multiphoton states compared to a classical light source<sup>22</sup>. The experimental sequence for performing a  $g^{(2)}(\tau)$  measurement starts by preparing the ion in the  $|\downarrow\rangle$  state using 422 nm  $\sigma^-$ -polarized light (Fig. 5). The ion is then excited using the  $\sigma^-$ -polarized 408 nm excitation pulse. We collect the subsequent  $P_{3/2}$  spontaneous emission into the HBT setup. A software gating window of 10 ns is applied to each time-tagger channel approximately 4.5 ns after the excitation pulse peak to exclude background counts arising from pulsed-laser light scattered from the ion trap and other surfaces. Then, since  $P_{3/2}$  decay has approximately a 1:16 branching ratio to  $D_{5/2}$ <sup>23</sup>, a 1033 nm quenching pulse removes any population trapped in  $D_{5/2}$ . Finally, we re-cool the ion with a 422 nm Doppler cooling pulse. The 1092 nm beam is applied continuously to clear out any population in  $D_{3/2}$ , since both  $P_{3/2}$  and  $P_{1/2}$  have branching ratios to this long-lived state<sup>23</sup>.

We use the Advanced Real-Time Infrastructure for Quantum physics (ARTIQ)<sup>24</sup> framework and Sinara hardware family to orchestrate the experimental sequence, including controlling the AOMs via RF switches (Minicircuits ZASWA-2-50DRA+). Our ARTIQ build is modified to include the Oxford Ion Trap group's Entangler Core<sup>25</sup>, allowing the data acquisition sequence to operate at a  $T_{\text{rep}} \approx 1250 \text{ ns}$  repetition period.

The raw coincidence counts distribution from a single ion obtained over 3 hours is shown in Fig. 6(a) using 1 ns bins. From the data, we can estimate the background-corrected  $g^{(2)}(0)$  following Ref. 26,

$$g^{(2)}(0) = \frac{C_0 - C_B}{C_\tau - C_B}, \quad (1)$$



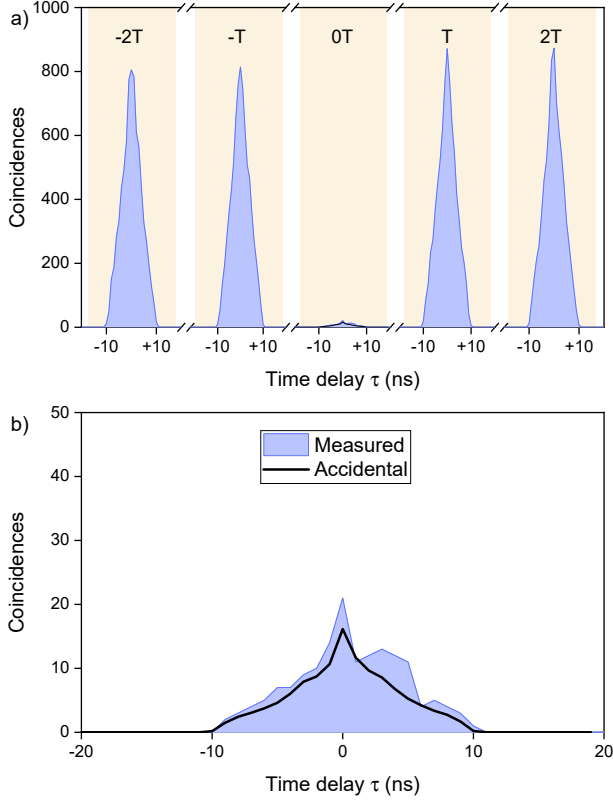


FIG. 6. Correlation measurement for a single ion over 3 hours of applying the pulse sequence using 1 ns bins. A 10 ns gated window after the excitation pulse is applied to remove most of the scattered background light. (a) Coincidence distribution showing four side peaks with a temporal spacing of  $T$  between each peak. (b) The coincidence distribution around  $\tau = 0$  is almost fully accounted for by the calculated contribution of the background (accidental coincidences), assuming perfect single photon emission from the ion.

The residual background count rate was measured for 5 minutes. For  $n$  independent emitters, the second-order correlation is given by<sup>28</sup>

$$g_n^{(2)}(0) = 1 - \frac{1}{n}. \quad (3)$$

Fig. 7 shows a plot of measured  $g_n^{(2)}(0)$  versus ion number after background subtraction and is consistent with  $n$  independent emission events per experimental cycle and uniform collection from the emitters. We note that most of the background contribution is due to scattered light from the excitation pulse. Assuming that the probability of  $m$  emission events  $P(m)$  from each ion is much smaller for multiple emission events compared to single events such that<sup>29</sup>  $P(1) \gg P(2) \gg P(> 2)$ ,  $g_n^{(2)}(0) \approx 2P(2)/P(1)^2$ . An upper-bound on the mean infidelity due to multiple emission events can be approximated by  $P(2)/P(1) \approx \frac{1}{2}P(1)g^{(2)}(0) = 2.55 \times 10^{-3}$  for a single ion. This upper-bound may be achieved by better spatial or temporal filtering of the excitation pulse.

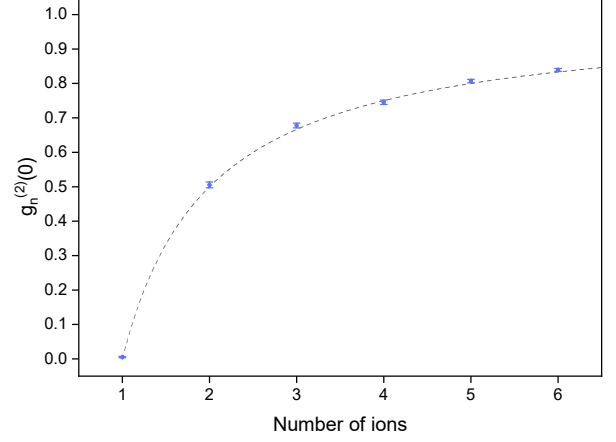


FIG. 7.  $g_n^{(2)}(0)$  as a function of ion number  $n$ . The  $g^{(2)}$  value was calculated using Eq. 1 and is consistent with the prediction of  $g_n^{(2)}(0) = 1 - 1/n$  (dashed gray line) for  $n$  independent emitters.

#### IV. CONCLUSION

In this paper, we report the development of an instrument to trap  $^{88}\text{Sr}^+$  ions and use them as a high-quality source of 408 nm photons. We describe the vacuum and laser systems, including a custom 150 ps pulsed laser system. We measured a  $g^{(2)}(0)$  for a single ion that is competitive with state-of-the-art photon sources. For strings of multiple ions, we report a  $g_n^{(2)}(0)$  consistent with independent emission by each ion. In the future,  $^{88}\text{Sr}^+$  ions trapped in multiple zones may be “remotely” entangled by collecting and interfering 408 nm light on the  $S_{1/2} \leftrightarrow P_{3/2}$  transition. By implementing one- and two-qubit gates in each zone, this system would realize an architecture for exploring distributed quantum computing<sup>4</sup> and entanglement distillation<sup>30,31</sup>.

## ACKNOWLEDGMENTS

This work was supported by funding from the National Science Foundation through the Quantum Leap Challenge Institute for Hybrid Quantum Architectures and Networks (QLCI-HQAN) (award number 2016136). This material is also based upon work supported by the U.S. Department of Energy Office of Science National Quantum Information Science Research Centers. The Q-NEXT center supported the multi-ion  $g_n^{(2)}(0)$  measurements. We acknowledge technical assistance from the MIT LL quantum computing group, including Felix Knollman and Susanna Todaro.

## AUTHOR DECLARATIONS

### Conflict of Interest

The authors have no conflicts to disclose.

### Author Contributions

**Jianlong Lin:** implemented the HBT setup and the experimental sequence for the  $g^{(2)}$  measurement, measured and processed the data for single and multiple ions, and contributed to writing the manuscript. **Mari Cieszynski:** designed and built the vacuum system, integrated the surface trap and wiring, and contributed to writing the manuscript. **William Christopherson:** designed and built the laser, imaging, control, and ion loading systems and contributed to writing the manuscript. **Darman Khan:** contributed to taking and analyzing data for single and multiple ions. **Lintao Li:** designed and built the 674 nm injection lock and pulsed laser systems. **Elizabeth Goldschmidt:** contributed to the design of the experiment and the writing of the manuscript. **Brian DeMarco:** contributed to the design of the experiment and the writing of the manuscript.

## DATA AVAILABILITY STATEMENT

The data that support the findings of this study are available from the corresponding author upon reasonable request.

### Appendix A: Pulse generation circuit

A schematic of the circuit that drives the 816 nm EOM is shown in Fig. 8. The circuit uses the fast switching transition of a step-recovery diode (SRD) (Macom MMD837) to begin the pulse. The rising edge voltage is split, propagating to the output along a transmission line. After the transmission line, a short circuit inverts the voltage and it is reflected back along the transmission line. Finally, the inverted transition edge recombines with the initial edge to terminate the pulse. Before pulse generation, SRD D2 is forward biased by

transistor Q4, which acts as a negative current source. Diode D1 is initially reverse biased. A pulse sent to the trigger input (J2) is amplified to 10 V by transistors Q1, Q2, and Q3. The trigger pulse passes through C5 and reverse biases SRD D2, which switches with a transition time of 60 ps and generates the rising edge of the pulse. The rising edge propagates to the output J3 and back along the transmission line TL1. D1 acts as a short to this positive voltage such that a negative-going reflection propagates back along TL1, thereby bringing the voltage at the output back to zero and terminating the output pulse. The transmission line length is set by the placement of the SRD on the printed circuit board and determines the pulse duration. For the pulse used in this work, TL1 is 1 cm long.

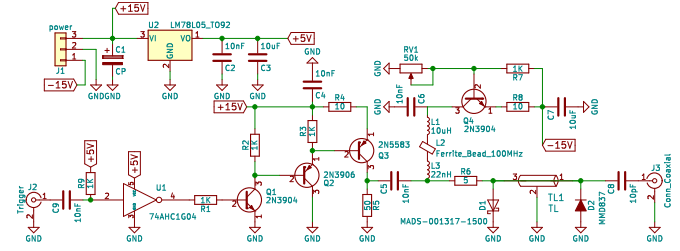


FIG. 8. Circuit used to generate voltage pulses applied to the 816 nm EOM.

## Appendix B: 408 nm pulsed laser system feedback

### 1. 816 nm EOM temperature stabilization

To achieve high-contrast pulses at 816 nm, we separately stabilize the birefringence of the EOM and the input/output optical fibers via temperature control. Two independent feedback systems sample the light transmitted by the PBS that follows the EOM output fiber. The control systems are designed to minimize the transmitted optical power at zero applied voltage. They are able to operate continuously, since the low duty cycle during data collection results in an average 816 nm power that is much smaller than the minimal static leakage. Furthermore, the experiment operates at a repetition rate that is incommensurate with the modulation frequency used for locking.

The EOM temperature and the optical fiber temperature are actively stabilized with feedback to two thermo-electric coolers (TECs): one mounted on the EOM body, and one which controls the temperature of the input/output fibers. The blue block of Fig. 4 shows how the control signal is generated and applied to the EOM TEC. A fraction of the output power is sent to a photodiode with a 1 M $\Omega$  trans-impedance amplifier gain. Lock-in detection is used for stabilizing the temperature by introducing a small 8 Hz modulation signal that is mixed with the photodiode signal and combined into the EOM AC modulation port through a bias-tee.

Similar to the EOM temperature feedback system, we control the birefringence of the polarization-maintaining fibers by adjusting temperature (magenta block of Fig. 4). The EOM



input and output optical fibers are taped to a copper plate that is temperature controlled by a TEC. The frequency of fiber-temperature modulation is approximately 20 mHz, which is sufficiently separated from the EOM modulation at 8 Hz such that the two feedback stages are decoupled. Together, the stabilized system provides a 31 dB extinction ratio, that is squared (on a linear scale) by the doubling stage's power threshold.

## 2. Tapered amplifier gain stabilization

We have observed that the 408 nm pulse shape and peak power are affected by the 816 nm TA current. To optimize for peak power and minimum pulse length, we adjust the TA current based on a feedback system. This control system is designed to maximize the power of the 408 nm light that results from frequency doubling the 816 nm EOM leakage at zero applied voltage. The feedback system is able to operate continuously because of the low duty cycle of the 408 nm pulse during data collection.

For this feedback system, we make use of the modulation applied to the EOM voltage. As described in Appendix B 1, an 8 Hz modulation signal is applied to the EOM AC input. When the EOM temperature control systems are locked, this modulation signal is rectified in the EOM output power and doubled 408 nm power such that the frequency is doubled to 16 Hz. The green block in Fig. 4 outlines the TA gain feedback circuit that uses this 16 Hz signal.

A fraction of the doubled 408 nm light is picked off and measured by a photodiode with a 10 M $\Omega$  transimpedance amplifier gain. The 16 Hz signal has poor signal-to-noise ratio, so it is filtered using a band-pass. A PID controller uses this signal to control the TA gain by adjusting the TA current. Similar to the EOM temperature servo, this feedback loop is not affected by the pulse train as long as the experiment avoids a repetition rate commensurate with 16 Hz.

<sup>1</sup>D. P. DiVincenzo, "The physical implementation of quantum computation," *Fortschritte der Physik* **48**, 771–783 (2000).

<sup>2</sup>H. J. Kimble, "The quantum internet," *Nature* **453**, 1023–1030 (2008).

<sup>3</sup>J. P. Covey, H. Weinfurter, and H. Bernien, "Quantum networks with neutral atom processing nodes," *npj Quantum Information* **9**, 90 (2023).

<sup>4</sup>D. Main, P. Drmota, D. P. Nadlinger, E. M. Ainley, A. Agrawal, B. C. Nichol, R. Srinivas, G. Araneda, and D. M. Lucas, "Distributed quantum computing across an optical network link," *Nature* **638**, 383–388 (2025).

<sup>5</sup>E. B. Flagg, S. V. Polyakov, T. Thomay, and G. S. Solomon, "Dynamics of nonclassical light from a single solid-state quantum emitter," *Physical review letters* **109**, 163601 (2012).

<sup>6</sup>M. Esmann, S. C. Wein, and C. Antón-Solanas, "Solid-state single-photon sources: Recent advances for novel quantum materials," *Advanced Functional Materials* **34**, 2315936 (2024).

<sup>7</sup>A. Liu, S. T. Cundiff, D. B. Almeida, and R. Ulbricht, "Spectral broadening and ultrafast dynamics of a nitrogen-vacancy center ensemble in diamond," *Materials for Quantum Technology* **1**, 025002 (2021).

<sup>8</sup>G. Andriani, F. Amanti, F. Armani, V. Bellani, V. Bonaiuto, S. Cammarata, M. Campostrini, T. H. Dao, F. De Matteis, V. Demontis, G. Di Giuseppe, S. Ditalia Tchernij, S. Donati, A. Fontana, J. Forneris, R. Francini, L. Frontini, R. Gunnella, S. Iadanza, A. E. Kaplan, C. Lacava, V. Liberali, F. Marzioni, E. Nieto Hernández, E. Pedreschi, P. Piergentili, D. Prete, P. Proposito, V. Rigato, C. Roncolato, F. Rossella, A. Salamon, M. Salvato, F. Sargeni, J. Shojaii, F. Spinella, A. Stabile, A. Toncelli, G. Trucco,

and V. Vitali, "Solid-state color centers for single-photon generation," *Photonics* **11** (2024), 10.3390/photonics11020188.

<sup>9</sup>R. Waltrich, M. Klotz, V. N. Agafonov, and A. Kubanek, "Two-photon interference from silicon-vacancy centers in remote nanodiamonds," *Nanophotonics* **12**, 3663–3669 (2023).

<sup>10</sup>C. D. Bruzewicz, J. Chiaverini, R. McConnell, and J. M. Sage, "Trapped-ion quantum computing: Progress and challenges," *Applied Physics Reviews* **6**, 021314 (2019).

<sup>11</sup>J. M. Sage, A. J. Kerman, and J. Chiaverini, "Loading of a surface-electrode ion trap from a remote, precooled source," *Physical Review A* **86**, 013417 (2012).

<sup>12</sup>C. D. Bruzewicz, R. McConnell, J. Chiaverini, and J. M. Sage, "Scalable loading of a two-dimensional trapped-ion array," *Nature Communications* **7**, 13005 (2016).

<sup>13</sup>W. Huie, L. Li, N. Chen, X. Hu, Z. Jia, W. K. C. Sun, and J. P. Covey, "Repetitive readout and real-time control of nuclear spin qubits in  $^{171}\text{Yb}$  atoms," *PRX Quantum* **4**, 030337 (2023).

<sup>14</sup>J. Chiaverini and J. M. Sage, "Insensitivity of the rate of ion motional heating to trap-electrode material over a large temperature range," *Phys. Rev. A* **89**, 012318 (2014).

<sup>15</sup>X. Shi, J. Sinanan-Singh, K. DeBry, S. L. Todaro, I. L. Chuang, and J. Chiaverini, "Long-lived metastable-qubit memory," (2024), *eprint*: 2408.00975.

<sup>16</sup>A. Keselman, Y. Glickman, N. Akerman, S. Kotler, and R. Ozeri, "High-fidelity state detection and tomography of a single-ion zeeman qubit," *New Journal of Physics* **13**, 073027 (2011).

<sup>17</sup>A. Shiner, *Development of a Frequency Stabilized 422-nm Diode-laser System and Its Application to a Strontium-88 Single Ion Optical Frequency Standard*, *mathesis*, York University (2006).

<sup>18</sup>F. Knollman, E. Clements, K. DeBry, S. L. Todaro, I. L. Chuang, and J. Chiaverini, "Private communication," (2024), *eprint*: 2408.00975.

<sup>19</sup>J. E. Sansonetti, "Wavelengths, transition probabilities, and energy levels for the spectra of strontium ions (sr ii through sr xxxviii)," *Journal of Physical and Chemical Reference Data* **41**, 013102–013102–119 (2012).

<sup>20</sup>M. Brownnutt, *88Sr+ ion trapping techniques and technologies for quantum information processing*, Ph.D. thesis, Imperial College London (2007).

<sup>21</sup>L. Zou, S. Gupta, and C. Caloz, "A simple picosecond pulse generator based on a pair of step recovery diodes," *IEEE Microwave and Wireless Components Letters* **27**, 467–469 (2017).

<sup>22</sup>R. Loudon, *The Quantum Theory of Light* (Oxford University Press, 2000).

<sup>23</sup>H. Zhang, M. Gutierrez, G. H. Low, R. Rines, J. Stuart, T. Wu, and I. Chuang, "Iterative precision measurement of branching ratios applied to  $5p$  states in  $88\text{Sr}^+$ ," *New Journal of Physics* **18**, 123021 (2016).

<sup>24</sup>S. Bourdeauducq, Whitequark, R. Jördens, D. Nadlinger, Y. Sionneau, and F. Kermarrec, "Artiq," (2021).

<sup>25</sup>D. Risinger, "Entangler core," <https://github.com/OxfordIonTrapGroup/entangler-core> (2021).

<sup>26</sup>R. H. Hadfield, M. J. Stevens, R. P. Mirin, and S. W. Nam, "Single-photon characterization with twin infrared-sensitive superconducting single-photon detectors," *Journal of Applied Physics* **101**, 103104 (2007).

<sup>27</sup>N. Lo Piparo, W. J. Munro, and K. Nemoto, "Quantum multiplexing," *Phys. Rev. A* **99**, 022337 (2019).

<sup>28</sup>E. Suarez, D. Auwärter, T. J. Arruda, R. Bachelard, P. W. Courteille, C. Zimmermann, and S. Slama, "Photon-antibunching in the fluorescence of statistical ensembles of emitters at an optical nanofiber-tip," *New Journal of Physics* **21**, 035009 (2019).

<sup>29</sup>M. J. Stevens, "Chapter 2 - photon statistics, measurements, and measurements tools," in *Single-Photon Generation and Detection*, *Experimental Methods in the Physical Sciences*, Vol. 45, edited by A. Migdall, S. V. Polyakov, J. Fan, and J. C. Bienfang (Academic Press, 2013) pp. 25–68.

<sup>30</sup>A. Kang, S. Guha, N. Rengaswamy, and K. P. Seshadreesan, "Trapped ion quantum repeaters with entanglement distillation based on quantum ldpc codes," in *2023 IEEE International Conference on Quantum Computing and Engineering (QCE)*, Vol. 01 (2023) pp. 1165–1171.

<sup>31</sup>M. Vitoria, S. Tserkis, S. Krastanov, A. S. de la Cerdá, S. Willis, and P. Narang, "Entanglement purification on quantum networks," *Phys. Rev. Res.* **5**, 033171 (2023).